

Rev. Sci. Instrum. 95, 013301 (2024) https://doi.org/10.1063/5.0174672

RESEARCH ARTICLE | JANUARY 05 2024







16 July 2024 18:59:36

Preliminary searches for spin-dependent interactions using sidebands of nuclear spin-precession signals

Cite as: Rev. Sci. Instrum. 95, 013301 (2024); doi: 10.1063/5.0174672 Submitted: 1 September 2023 • Accepted: 10 December 2023 • Published Online: 5 January 2024







Published Online: 5 January 2024

J. Shortino, D. S. Knappe-Grueneberg, D. Voigt, D. P.-H. Chu, D. A. Reid, D. W. M. Snow, D. D. Voigt, D. P.-H. Chu, D. A. Reid, D. W. M. Snow, D. D. Voigt, D. P.-H. Chu, D. D. Chu, D. Chu,

AFFILIATIONS

and W. Kilian^{2,a)}

- Department of Physics, Indiana University, Bloomington, Indiana 47405, USA
- ²Physikalisch-Technische Bundesanstalt (PTB), 10587 Berlin, Germany
- Los Alamos National Laboratory, Los Alamos, New Mexico 87545, USA

ABSTRACT

Various theories beyond the Standard Model predict new particles with masses in the sub-eV range with very weak couplings to ordinary matter. A new P-odd and T-odd interaction between polarized and unpolarized nucleons proportional to $\vec{s} \cdot \hat{r}$ is one such possibility, where $\vec{r} = r\hat{r}$ is the spatial vector connecting the nucleons, and \vec{s} is the spin of the polarized nucleon. Such an interaction involving a scalar coupling g_s^N at one vertex and a pseudoscalar coupling g_p^n at the polarized nucleon vertex can be induced by the exchange of spin-0 pseudoscalar bosons. We describe a new technique to search for interactions of this form and present the first measurements of this type. We show that future improvements to this technique can improve the laboratory upper bound on the product $g_s^N g_p^n$ by two orders of magnitude for interaction ranges at the 100 micron scale.

Published under an exclusive license by AIP Publishing. https://doi.org/10.1063/5.0174672

I. INTRODUCTION

The possible existence of new interactions in nature with sub-millimeter ranges, corresponding to exchange boson masses above 1 meV and with very weak couplings to matter, has been discussed for some time. 1-3 The extended symmetries present in many theories beyond the Standard Model⁴ are typically broken at some high energy scale, leading to weakly coupled light particles with relatively long-range interactions.⁵ The Goldstone theorem in quantum field theory guarantees that the spontaneous breakdown of a continuous symmetry at scale M leads to a massless pseudoscalar mode with weak coupling g to massive fermions m of order g = m/M. The mode can then acquire a light mass (thereby becoming a pseudo-Goldstone boson) of order $m_b = \Lambda^2/M$ if there is also an explicit breaking of the symmetry 6 at scale Λ . For example, the axion, which was proposed to explain the strong charge-parity (CP) problem⁷ and can generate spin-dependent interactions, can be introduced through spontaneous symmetry breaking. The axion mass m_a can be determined as $m_a \approx 6 \text{ eV} \frac{10^6 \text{ GeV}}{f_a}$, where f_a is the axion decay constant related to the breaking energy scale.

In this paper, we focus on one such possibility: a new interaction from the exchange of a spin-0 pseudoscalar boson. Motivated by their search for new methods to look for axions, Moody and Wilczek⁹ considered what new macroscopic forces could be induced by axion exchange between and among electrons and nucleons. They drew attention to the parity (P)-odd and time reversal (T)-odd potential of the form,

$$V_{9+10} = g_{s}^{N} g_{p}^{n} \frac{\hbar^{2}}{8\pi m_{\dagger}} (\hat{\sigma}_{i} \cdot \hat{r}) \left(\frac{1}{\lambda r} + \frac{1}{r^{2}} \right) e^{-r/\lambda}, \tag{1}$$

referred to as a "monopole–dipole" potential, where $g_s^N g_p^n$ is the total coupling strength of this interaction to the spin-0 boson. g_s^N is the scalar coupling constant to an unpolarized nucleon, g_p^n is the pseudoscalar coupling constant to a polarized nucleon with its

a) Author to whom correspondence should be addressed: wolfgang.kilian@ptb.de

mass m_{\uparrow} (neutron in the case of $^{129}\mathrm{Xe}$), λ is the interaction length, $\hat{\sigma}_i$ are the Pauli matrices belonging to the spin of the polarized particle, and r is the distance between the polarized particle and the unpolarized particle. Subsequent theoretical work 10,11 recovered the monopole–dipole potential as one of 16 linearly independent non-relativistic potentials from the single exchange of a spin-0 or spin-1 boson composed of scalar invariants involving the spins, momenta, interaction range, and possible particle couplings between nonrelativistic spin-1/2 fermions. A recent review and a book chapter have placed this work in the context of analogous investigations using atomic measurements.

II. SHORT-RANGE MONOPOLE-DIPOLE INTERACTION EXPERIMENTS

The axion interaction on the spin $\hat{\sigma}_i$ with gyromagnetic ratio γ acts on particle spins such as a pseudo-magnetic field \vec{B}_a : $V_{9+10} = \Delta E_a = h\Delta v_a = \gamma\hbar\hat{\sigma}_i \cdot \vec{B}_a$, where ΔE_a is the energy shift of the corresponding spin state leading to a change in the transition frequency $2\Delta v_a$ between two states with opposite spin orientation. When modulated, \vec{B}_a can act on the longitudinal magnetization such as a classical B_1 NMR-field 14,15 (largest when $B_a \perp B_0$), or it can modulate the Larmor precession frequency of the spins 16,17 (largest when $B_a \parallel B_0$).

Two primary factors cause the existing experimental constraints on monopole-dipole interactions to degrade rapidly for distance scales below 1 cm (as shown in Fig. 5). First, for shorter-range interactions, the number of spin-polarized particles that can be brought within the relevant interaction range becomes smaller and smaller. In addition, it becomes more and more difficult to maintain the required precision of the systematic background effects from magnetic field distortions generated by test mass susceptibility and magnetic impurities.

For several reasons, ensembles of polarized noble gas atoms such as ${}^3\mathrm{He}, {}^{14,18-20}$ ${}^{129}\mathrm{Xe}, {}^{19,21,22}$ and ${}^{131}\mathrm{Xe}, {}^{21,22}$ have been employed to extend the search for monopole–dipole interactions to shorter distance scales. The technology of laser optical pumping produces macroscopic quantities of these atoms with high nuclear polarization. The weak interactions of the chemically inert, closed electron shells of noble gas atoms help to isolate the nuclei from competing external influences. Polarized noble gas technology has undergone extensive development for a wide variety of scientific applications in neutron scattering, medical imaging, and nuclear and particle physics ${}^{23-25}$

Single-species magnetometers require extreme care to reduce possible interference from stray magnetic fields, as it is difficult to distinguish magnetic influences from potential axion-related effects. A combined ³He-¹²⁹Xe system allows one to treat one of the polarized species as the system to search for the monopole-dipole field and the other to act as a co-magnetometer. This is possible since the response of different polarized nuclei to the monopole-dipole potential will not be the same. In the case of ³He, experimental measurements and theoretical calculations agree²⁶ that, to an excellent approximation, the polarization of the ³He nucleus is dominated as one would expect by the polarization of the neutron, and, therefore, any limit derived from monopole-dipole interactions in this system can be directly attributed to a limit on neutron interactions. Theoretical calculations of the neutron spin contribution to

the nuclear angular momentum have also been performed for $^{129}\mathrm{Xe}$ and $^{131}\mathrm{Xe}.^{27,28}$

One method is to simply measure the precession frequency of the gas with the mass nearby or far away. The mass provides the nucleons for the monopole–dipole potential. When the mass position is moved relative to the cell, the interaction strength changes between the mass and the spins. Any deviation in the resultant Larmor frequency could indicate the presence of an axion field. This method was pursued in various experiments ^{18,19,21,22} with success.

Another approach under development will use a rotating sprocket wheel as a test mass to modulate the monopole–dipole field perpendicular to a static magnetic holding field. If the frequency of the sprockets coming close to the polarized ³He spins matches the nuclear precession frequency, one can resonantly couple the monopole–dipole field energy into the nuclear spin system and thereby tilt the total spin magnetization. The corresponding transverse magnetization produced by the induced spin precession is then measured by a sensitive magnetometer. This method was proposed by Arvanitaki and Geraci and is the concept of the Axion Resonant InterAction Detection Experiment (ARIADNE). ^{14,20}

In this paper, we discuss another experimental approach, the Axion Noble Gas Interaction in the Short-Range (ANGIS), a frequency-modulated (FM) sideband magnetometry experiment following our idea of the "SIdeband in Larmor Frequency Induced by Axions" (SILFIA) method. 16 To do so, we employ a rotor with incorporated unpolarized germanium masses of high density in front of a sample of spin-polarized $^{129}\mathrm{Xe}$ gas ensemble precessing about a static magnetic holding field. Therefore, the $^{129}\mathrm{Xe}$ spins are subjected to a frequency-modulated V_{9+10} monopole–dipole interaction, producing frequency modulation on the Larmor frequency.

III. SIDEBAND SIGNALS FROM FREQUENCY MODULATION

Generally, when the frequency of a sinusoidal signal is periodically symmetrically modulated away from its center frequency f_c and analyzed by a Fourier transform, additional peaks appear separated in frequency by kf_m (with $k \in \mathbb{N} \geq 1$) away from f_c and equally spaced by the modulation frequency f_m , i.e., the inverse time needed for the complete frequency sweep. These peaks are known as sideband signals. The maximum change of the frequency away from f_c is the modulation depth $\Delta f = 0.5(f_{\text{max}} - f_{\text{min}})$. A frequency-modulated signal has a time-dependent frequency, as given by

$$\omega(t) = 2\pi f(t) = 2\pi (f_c + \Delta f \cos(2\pi f_m t)). \tag{2}$$

The associated signal is calculated by integrating and taking the cosine,

$$S_{\rm x}(t) \propto \cos\left(\int \omega(t)dt\right) = \cos\left(2\pi f_{\rm c}t + \frac{\Delta f}{f_{\rm m}}\sin\left(2\pi f_{\rm m}t\right)\right).$$
 (3)

To understand the sideband signals in the frequency domain, the time domain signal can be converted into the sum of cosines,

$$S_{\rm x}(t) \propto \sum_{k=-\infty}^{\infty} J_k \left(\frac{\Delta f}{f_{\rm m}}\right) \cos\left(2\pi (f_{\rm c} + k f_{\rm m})t\right),$$
 (4)

where the cosine coefficients $J_k\left(\frac{\Delta f}{f_{\rm m}}\right)$ are the Bessel functions. These coefficients are proportional to the amplitudes A_k of the corresponding FM sidebands in the frequency domain at $f_k = f_c \pm k f_{\rm m}$.

For small modulations where $\Delta f \ll f_{\rm m}$, the ratio of the first-order sideband amplitude $A_{\rm l}$ to the central peak amplitude $A_{\rm c}$ is approximated as

$$\frac{A_1}{A_c} \approx \frac{\Delta f}{2f_{\rm m}}.$$
 (5)

We have checked numerically that when $\frac{\Delta f}{f_{\rm m}} < 10^{-3}$, as was the case in our experiments, the approximation is accurate to the 10^{-7} level.

IV. EXPERIMENTAL SETUP

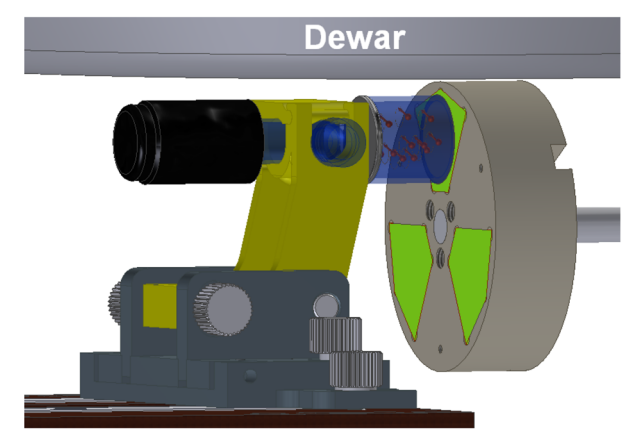
All experiments were performed inside the Berlin Magnetically Shielded Room-2 (BMSR-2) at the Physikalisch–Technische Bundesanstalt (PTB), Institute Berlin, similar to previous experiments. $^{19,29-31}$

A. Berlin Magnetically Shielded Room-2

After an upgrade phase between 2018 and 2020, BMSR-2 consists of eight Mu-Metal layers and one aluminum layer. The magnetic shielding factor was measured³² to be more than 7×10^7 at 10 Hz. The spin precession was measured by one SQUID (Superconducting Quantum Interference Device) of a multichannel vector system, housed in non-magnetic Dewars made of glass fiber-reinforced plastics. This SQUID system has been used in several experiments searching for exotic physics. 19,29-31 The distance between the lowermost sensor used for the spin-precession detection and the lower Dewar surface is 28 mm and gives rise to a magnetic noise level of about 3 fT/ $\sqrt{\text{Hz}}$ around the two relevant frequencies of 2.5 and 32 Hz. To generate the B_0 -field as well as the AC-excitation $(B_1$ -field) for initiating the spin precession, a system of three crossed Helmholtz coils with 1.6 m (B_0) , 1.5, and 1.4 m (B_1) , respectively, was centered relative to the magnetic center of the BMSR-2. The overall magnetic field gradients are in the order of 20 pT/cm at $B_0 = 2 \mu T$. A complex tower to hold the gas sample cell, as well as the wheel with the masses, was constructed and set underneath the SQUID Dewar such that the gas cell was fixed in the center of the coil system. The cell holder allowed fine adjustments such that the thinwalled window of the cell could be aligned in parallel to the wheel's flat face, shimmed either by a piece of paper (80 μ m) or plastic spacer blocks of known thickness. Prior to measurement, the spacer was removed [Fig. 1(a)].

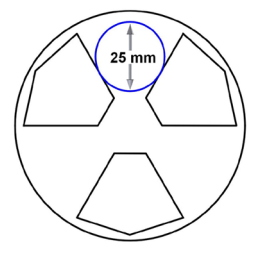
B. Gas sample cell

Dedicated measurement cells are necessary to confine and hermetically seal hyperpolarized 129 Xe or other rare gases, as was the case in other precision experiments utilizing hyperpolarized rare gases. 19,30,31 One limitation in our primary experimental search for a short-range spin-dependent interaction rapidly decreasing with distance [Eq. (1)] was the utilization of a cylinder cell with relatively thick windows 19 (\approx 2 mm). Another previous experiment 18 used hemispheric sub-mm "windows" at the cylinder ends, utilizing a rather high pressure (7 amagat); however, due to the sphericity,



(a) Schematic of the central setup.





(b) Gas Sample Cell WK06

(c) Wheel rotated 60°

FIG. 1. Schematic of the experimental setup located in the center of BMSR-2, with the gas sample cell (blue-transparent with red spin arrows inside) adjacent to the rotating wheel (gray) incorporating the three source masses (green), both below the Dewar (gray shaded), which contains the SQUIDs (a). Image of one of our sample cells for storing the hyperpolarized $^{129}\mathrm{Xe}$ gas (b). Sketch of the position of the cell (blue circle) relative to the test masses when the wheel is rotated by 60° (c). The external B_0 holding field is oriented along the cell axis.

only a very small portion of the detected precessing spin-polarized gas had the ability to probe the very short distances overall, reducing the sensitivity. To allow for the highest sensitivity, the cylinder cell with flat, thin windows has to maximize the nuclear spin-relaxation time while minimizing frequency shifts due to the magnetization of the hyperpolarized gas itself. A cylindrical cell with a height-to-diameter ratio of 0.9065 has been shown to eliminate self-frequency shifts.³³ To maximize relaxation times, our cells need to be baked under a vacuum for inner wall surface cleaning. Hence, we had to determine how thin a cylindrical window with an unsupported diameter on the cm scale could be while still supporting at least one bar of pressure difference.

Materials such as glass¹⁹ or silicon,³¹ as well as Al_2O_3 , were previously used in-house and known to be suitable, if treated correctly, regarding the spin relaxation properties of the walls. Thus, we tested Si wafers as well as precision sapphire windows. By putting disks of those materials on top of an O-ring with comparable diameters as the disks and by applying a vacuum from underneath, burst-proof tests were performed. We successfully tested 50.8 mm diameter sapphire (silicon) wafers with 0.3 mm (0.625 mm) thickness, respectively. In addition, a 25.4 mm diameter silicon wafer with

just 0.15 mm thickness did not break but instead bowed considerably when the vacuum was applied from one side. Thus, we have decided to use a sapphire window on one side of a Duran glass cylinder with a precision inner diameter of 25 mm and a length of 22.675 mm. As the hyperpolarized gas had to be refilled, we built the cell with a 3.3 mm thick window comprising a central 1 mm diameter hole on the opposite side. A glass valve with a PTFE (Polytetrafluoroethylene) stopcock was cut and put on top of the hole in the thick window, such that almost no dead volume emerged. The joining was done by simply stacking all four elements on each other and applying Loctite® EA-1C high viscosity glue from the outside to the connecting grooves; see Fig. 1(b). This cell showed ¹²⁹Xe longitudinal spin relaxation times of $T_1 \approx 150$ minutes at a 3 mT holding field. Another cell with somewhat smaller dimensions (ID = 20.00 mm, l = 18.14 mm, and a silicon window of 0.625 mm) was also made and used for the experiments.

C. Test mass design and movement

The axion-mediated potential [Eq. (1)] experienced by a spinpolarized sample is proportional to the nucleon density of the nearby mass. Our three test masses were incorporated into a Polyoxymethylene (POM) wheel and consisted of pentagon-shaped germanium blocks. The wheel is rotated between positions where germanium or POM is near the cell [Fig. 1(a)].

POM was chosen as the housing material as its volume susceptibility is close to that of germanium but has a substantially lower nucleon density. To compare the susceptibilities of the Ge test mass and different plastic materials for the wheel, MPMS measurements (SQUID-based Magnetic Property Measurement System) were

TABLE I. Density and measured susceptibility of various materials.

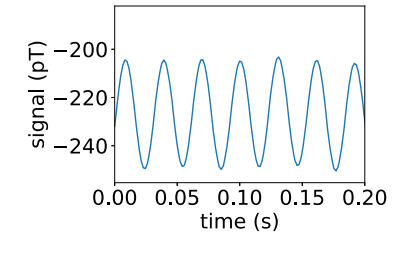
	ρ (g/cm ³)	$\chi_{\rm v} (10^{-6} \rm ppm)$
Germanium	5.32	-7.50
POM	1.41	-9.36
PEEK	1.32	-9.34
PE	0.92	-10.49
Air	0.001 23	0.36

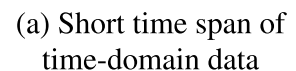
performed at PTB (see Table I). A larger difference in density variation would have been achieved by using empty (air-filled) segments instead of full POM material; however, this would have increased the systematic susceptibility artifact. The germanium was cut from single crystals. The choice of single-crystal material was made with the hope that the same procedures used to create the single crystal would also help to reduce the concentration of (possibly magnetic) impurities. All parts of the setup and the Ge test masses were cleaned carefully, checked for magnetic contamination, and degaussed before assembling. In an initial measurement with a pure POM wheel in front of the cell, no side bands were present; however, the same measurement at the end of our campaign did show sidebands, implying that magnetic impurities were incorporated into the setup.

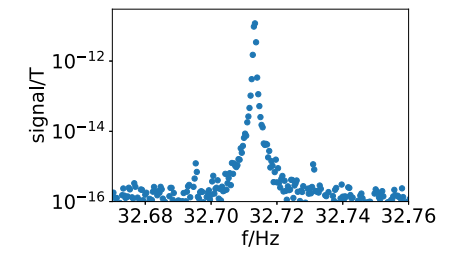
The rotation of the test mass wheel was operated by a non-magnetic pneumatic motor (a special ferrite-free version of the pmo450, PTM Mechatronics, Germany) at the bottom of the cell-mass tower, both of which were interconnected with a set of gears for translating the rotation. By regulating the pneumatic pressure from outside the BMSR-2, a control system driven by a computer control program had the ability to adjust both the speed and direction of rotation. Hold and movement times were recorded via an encoder slide fixed to the wheel axis.

V. MEASUREMENT DESCRIPTION

A series of test measurements were taken in BMSR-2 using the measurement set-up as shown in Fig. 1(a). The most sensitive measurements were taken with the WK06 cell [Fig. 1(b)] filled with a gas mixture of \approx 1.2 bar total pressure containing hyperpolarized enriched ¹²⁹Xe (80%) at a partial pressure of 150 mbar aside from the buffer gases nitrogen and helium as used within the ¹²⁹Xe polarizer. ³⁴ For an individual measurement, a cell of polarized ¹²⁹Xe gas was transported from the polarizer lab within a battery-powered solenoid ²⁹ and placed inside the BMSR-2 in front of the wheel containing the source masses with a known separation and was held in a known stable magnetic field B_0 (\approx 0.21 μ T and \approx 2.7 μ T with drifts below 10 pT/h). For a short period (\approx 2 s), a transverse rotating magnetic field was resonantly applied to tilt the spin magnetization by 90° into the transverse plane, resulting in spin precession signals at Larmor frequencies either near 2.5 or 32 Hz being detected







(b) FFT of the 3000 seconds run.

FIG. 2. Example of data from one of the acquired runs. The mean frequency of this measurement is 32.46 Hz, and the mass modulation generates the sidebands 25 mHz away, as shown in the fast Fourier transform.

by the SQUID system with typical start amplitudes of ³⁵ 25 pT [see Fig. 2(a)].

During a measurement, the wheel containing the source masses was rotated between the two distinct positions (POM or germanium in front), as shown in Fig. 1. The wheel was briefly rotated until it reached one of the positions and was held for some time. Then it was rotated back to the prior position and held for an equal amount of time. The transition time was typically 2.5 s, with the total cycle lasting 40 or 56 s, resulting in a modulation frequency of $f_{\rm m}=25$ and 17.8 mHz, respectively. During a typical measurement lasting 3000 seconds, close to the typical transverse relaxation time of $T_2^*\approx 2800$ s, the mass-switching cycle was continuously repeated. (See the supplementary material for the deduction of why a measurement duration in thelength of T_2^* is giving the highest sensitivity.)

In order to extract the carrier and sideband amplitudes from the data, a Hanning window was applied to the full data before generating amplitude peak spectra via a set of DFTs (discrete Fourier transforms). For the measurements with a spin precession frequency of $\approx 32\,$ Hz using a sample rate 36 of 610.4 Hz, a total of 19 DFTs were calculated from the same data. Each consecutive DFT was performed on a subset of the same data by subsequently deleting one data point from the end of the $\approx 795\,$ k total sample points. Altering the number of time domain sample points before calculating the DFT shifts the frequency bins in the spectral data, and thus, by merging all 19 DFTs into one data set, one overcomes the scalloping loss caused by the spectral leakage effect and creates a smoothed representation, as shown in Fig. 2(b).

Sidelobes arise from the windowing when performing a DFT. The Hanning window is an appropriate compromise between the increase in noise level and the strong roll-off of the sidelobes. To avoid adding false effects, we ensured that the sidebands were far off from the carrier frequency, such that the sidelobes at the sideband position already fell below the noise level.

The central peak amplitude A_c and central frequency f_c were determined by applying a Gaussian fit-model to the joined DFT data,

$$\langle S_{\mathbf{x}}(f) \rangle = A_{\mathbf{c}} \times \exp\left(-\frac{(f - f_{\mathbf{c}})^2}{2w^2}\right),$$
 (6)

where w is the characteristic width. Based on simulated data, we found a Gaussian described the line-shape best when using a measurement time of only one T_2^{\star} and a windowing before the DFT calculation. Due to the high SNR, the fit parameters for the central peak were thus determined with high precision. However, due to the much smaller SNR of the sideband signals, their frequencies were not determined by a fit but rather calculated from the central frequency and the modulation frequency, $f_1 = f_c \pm f_m$. To determine the sideband amplitudes, a fit with a Gaussian model was applied only with the amplitude parameter A_1 as a free parameter, also using the linewidth from the central peak. For each fit, a covariance matrix was produced. The uncertainty for each peak was calculated, attempting to account for fitting with data that are not statistically independent due to merging the shifted Fourier transforms from the same data set. To do so, a correction factor C_{σ} was applied to the equation for standard deviation, $\sigma_i = C_{\sigma} \sqrt{\text{cov}_{i,i}}$, where $\text{cov}_{i,i}$ is the corresponding value of the covariance matrix. This was tested against two sets of simulated data, estimating the correction factor $C_{\sigma} = 2\sqrt{\frac{n_1-m}{n_0-m}}$ for our measurements at \approx 32Hz, where $n_0 = 30$ is the number of data points from each individual Fourier transform used for the fit (corresponding to a spectral range of 10 mHz restricting each fit to the region of interest), $n_1 = 19 * n_0$ is the number of all data points used, and m is the number of fit parameters.

Equation (5) holds only for a sinusoidal modulation, but for other modulation patterns, the energy transferred to the sidebands is different. Due to the geometry of our wheel design, the resulting modulation in our setup closely represents a square wave with a small transition period. Generally, a normalized square wave decomposed into sinusoids is given as

$$Sq(t) = \frac{4}{\pi} \sum_{n=1}^{\infty} \frac{1}{n} \sin(2\pi n f_{\rm m} t),$$
 (7)

showing that the square wave holds $4/\pi \approx 1.2732$ times more energy than the sine wave, thus the ratio of the sideband to central peak amplitudes as derived for a pure sinusoidal modulation as given in Eq. (5) has to be scaled,

$$\frac{A_1}{A_c} = \frac{4}{\pi} \frac{\Delta f}{2f_m}.$$
 (8)

To deduce the factor arising from our non-perfect square wave modulation, we calculated the phase evolution for a pure sine modulation as well as for our trapezoidal modulation and calculated the corresponding time domain signal using Eq. (3). From these synthetic signals, the amplitude ratios A_1/A_c were derived as described above by Fourier transformation, interpolation, and fitting. With transition times in the range of 10% of the modulation cycle, the increase in amplitude ratio is derived to be 1.27, just slightly smaller than for a perfect square wave modulation. It was also numerically proven that this holds for an exponentially decaying signal

As the modulation depth Δf is defined as $0.5(f_{\rm max}-f_{\rm min})$ and a potential axion interaction from the source mass would shift the Larmor frequency of the nuclei from $f_{\rm max}$ to $f_{\rm min}$ (or vice versa), only half of the V_{9+10} introduced frequency change $2\Delta \nu_a$ between the two spin states would be seen in the amplitude ratio. Therefore, we can assign V_{9+10} to the amplitude ratio for our parameters as

$$V_{9+10} = h\Delta v_a = h \frac{2f_{\rm m}}{1.27} \frac{A_1}{A_c},\tag{9}$$

allowing us to deduce the axion coupling $g_N^s g_N^p$ with the use of Eq. (1) from the sideband analysis.

VI. VOLUME INTEGRAL AXION INTERACTION STRENGTH

Similar to the previous experiments, 37,38 the Monte Carlo integration method is used to derive limits for the corresponding exotic spin-dependent interaction. First, one has to integrate the potential between the test mass volume and the detector cell volume. For each corresponding interaction length λ , the average contribution to the

potential in Eq. (1), from which the distance-dependent integration part of the potential can be calculated as

$$P_{9+10} = \frac{\int (\hat{\sigma}_{i} \cdot \hat{r}) \left(\frac{1}{\lambda r} + \frac{1}{r^{2}}\right) e^{-r/\lambda} d^{3}r}{\int d^{3}r}$$

$$= \frac{1}{\int d^{3}r} \int \left(\sigma_{z}\hat{z} \cdot \left(\sin \theta \cos \phi \hat{x} + \sin \theta \sin \phi \hat{y} + \cos \theta \hat{z}\right)\right)$$

$$\times \left(\frac{1}{\lambda \rho} + \frac{1}{\rho^{2}}\right) e^{-\rho/\lambda} \rho^{2} \sin \theta d\rho d\theta d\phi$$

$$= \sigma_{z} \frac{\int \left[-\left(\sin \theta \cos \theta\right) (\rho + \lambda\right)\right] dr' d\theta d\phi}{\int d^{3}r}, \qquad (10)$$

where ρ , θ , and ϕ are the radial distance, the polar angle, and the azimuthal angle, respectively, in the spherical coordinate between the points in the test mass and the detector cell, and $r' \equiv e^{-\rho/\lambda}$. σ_z is the Pauli matrix, and it yields an eigenvalue of +1 (or -1) when applied to the spin state of ¹²⁹Xe. To apply this method, 2²⁰ random point pairs had to be generated, where each pair consisted of a point in the volume of the test mass (Ge) and one in the measurement cell. Next, after summing, averaging, and normalizing with the test mass nucleon density N, the numerical integration of the distance-dependent part of the potential could be calculated by summing 2^{20} random point pairs as

$$P_{9+10} = N \frac{1}{2^{20}} \sum_{i}^{2^{20}} \left[-(\sin \theta_i \cos \theta_i)(\rho_i + \lambda) \right]. \tag{11}$$

As mentioned in Sec. IV C, our test sample was comprised of a POM wheel with three inlaid germanium pentagons, whose effects were all calculated by the Monte Carlo method. Thus, for the effective potential, the density difference between germanium, and POM $N_{\rm Ge}-N_{\rm POM}$ has to be used for $N=(3.182-0.843)\times 10^{30}~{\rm m}^{-3}$ in the calculation of P_{9+10} . Along with Eq. (9) the volume averaged potential $\langle V_{9+10}\rangle=g_N^sg_N^p\frac{\hbar^2}{8\pi m_\uparrow}P_{9+10}$ can be solved for the coupling constants in terms of experimentally derived peak amplitudes,

$$g_N^s g_N^p = \frac{2f_{\rm m}}{1.27} \frac{A_1}{A_c} \frac{16\pi^2 m_{\dagger}}{\hbar} \frac{1}{P_{9+10}}.$$
 (12)

VII. SYSTEMATIC FALSE-EFFECTS

Classical effects changing the volume average magnetic field $\langle B_0 \rangle$ over the measurement cell correlated with the rotation of the test-mass wheel would also introduce a frequency modulation on the detected spin precession signal and consequently generate sidebands, which might be interpreted as a false effect.

A temporal change in nearby non-magnetic materials, in our case, the change from Ge to POM with different susceptibilities, deforms the local magnetic field and implies a frequency shift $\gamma/2\pi\langle\Delta B_{\rm sus}\rangle$. Similarly, a magnetic spot-impurity sitting on the front of the test-mass wheel would generate $\gamma/2\pi\langle\Delta B_{\rm imp}\rangle$. Thus, the measured modulation depth Δf between the two wheel positions is the sum of all three effects,

$$\Delta f = \frac{1}{2} \left| \frac{\gamma}{2\pi} (\langle \Delta B_{\text{sus}} \rangle + \langle \Delta B_{\text{imp}} \rangle) + 2\Delta \nu_{\text{a}} \right|. \tag{13}$$

TABLE II. Sensitivity of Δf with respect to changes in the three effects described by Eq. (13) (× indicates sensitive to changes).

	$\Delta B_{ m sus}$	$\Delta B_{ m imp}$	$\Delta v_{\rm a}$
B_0 amplitude	×		
B_0 orientation		×	×
Test-mass separation	×	×	×
Different sets Ge/POM		×	

Variations of experimental parameters that have or have no influence on the susceptibility or impurity effect should allow us to differentiate between those and a potential axion interaction. For this, one may think of the variation of B_0 field strength, B_0 field orientation, free space distance between wheel and cell, and cell volume, using different sets of Ge/POM. As listed in Table II, these parameters are sensitive in different ways to the three parameters of Eq. (13). For example, variation in the B_0 field should not touch any spin-dependent new forces or the effect of magnetic impurities but should change the susceptibility effect, where its magnitude and orientation matter. A larger free space between the mass and the inner volume of the cell will reduce all three effects. The signs of $\Delta B_{\rm imp}$ and $\Delta \nu_a$ are unknown but should not depend on the B_0 orientation. This was utilized in a specific experimental design, as described in the supplementary material.

Prior to the experiments, a finite element simulation (FEM) was performed to quantify the expected susceptibility effect using COM-SOL Multiphysics®, applying the geometry of our setup and using the WK06 cell at its closest position (i.e., with a 0.1 mm separation). This has shown a linear dependence of the volume average magnetic field change $\langle \Delta B_{\rm sus} \rangle$ over the sample cell in dependence of the Ge susceptibility. For the change between POM and Ge, we determined a volume average field change of $\Delta f_{\rm sus}/B_0 \approx 1.6~\mu Hz/\mu T$.

Consequently, this linear dependence of Δf was seen in all our field dependent measurements when analyzing the modulation depths, while the intercept at $B_0 = 0$ can arise from the combination of any spin-dependent exotic forces and magnetic impurity

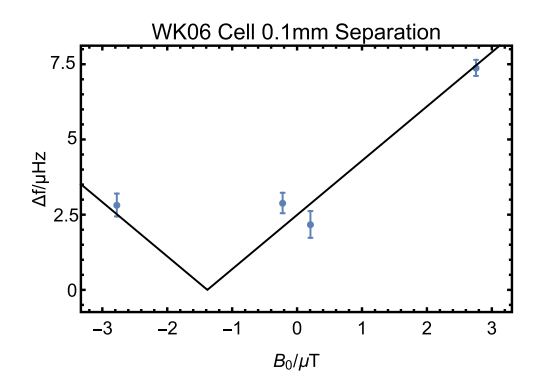


FIG. 3. Modulation depth Δf as defined in Eq. (13) of measurements taken with 0.1 mm separation between the WK06 cell and wheel and a linear fit to the function $|aB_0+b|$. The slope $a=(1.80\pm0.17)~\mu\text{Hz}/\mu\text{T}$ arises from magnetic susceptibility-related effects, while the y-offset $b=(2.49\pm0.37)~\mu\text{Hz}$ comes from any remaining magnetic impurity effects or other spin-dependent forces.

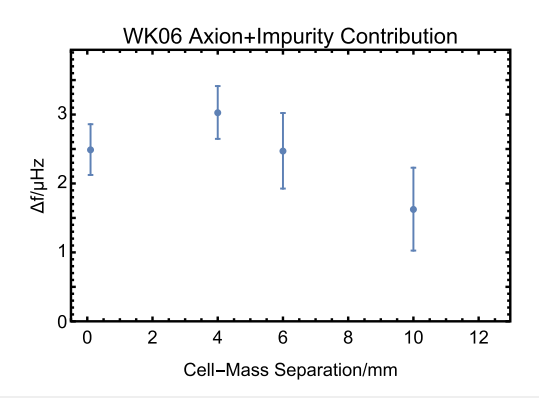


FIG. 4. Residual modulation depths after accounting for field-dependent effects. Each point in this figure is deduced from linear fits, as shown in Fig. 3. The best-fit y-intercept with uncertainty at $B_0=0$ in Fig. 3 is plotted by the left-hand most data point at 0.1 mm in this figure.

effects (see Fig. 3 and three more in the supplementary material). For this measurement, the sum of all spin-dependent effects is zero for $B_0 \approx -1.4~\mu\text{T}$, with the susceptibility effect equal and opposite to all impurity and axion-related interactions. The derived slopes from the two measurements with two different sets of POM and Ge positions using a WK06 cell close to the wheel were $(1.80 \pm 0.17)~\mu\text{Hz}/\mu\text{T}$ and $(1.58 \pm 0.16)~\mu\text{Hz}/\mu\text{T}$, both in good agreement with the value derived from the FEM simulation.

We compare the resulting field-independent effects by varying the separation between the cell and mass, as shown in (Fig. 4). The distance-relationship of a typical magnetic dipole impurity with a $1/r^3$ scaling and the effect from the axion will differ, with the axion potential having the Yukawa falloff of Eq. (1). However, due to insufficient data at distance scales below 4 mm, we were not able to discern the axion-related effects of a magnetic impurity. With a more thorough elimination of magnetizable spots on the test-mass wheel beforehand and measurements at even greater distances, this should be possible.

VIII. PROJECTED SENSITIVITY

The sensitivity of a sideband measurement primarily depends on the separation from the source mass and the gas nuclei, the SNR of the sidebands, and the effects of magnetic impurities. Source mass density and geometry, gas density, gas polarization, relaxation time, and measurement time will all contribute to the overall sensitivity. To best estimate the possible sensitivity of a sideband-style axion measurement, we will consider the results of ANGIS with a few improvements. The first improvement assumes a source mass without any magnetic impurities or another method for mitigating the effects of any magnetic impurities. These effects could be mitigated through magnetic shielding, the use of a co-magnetometer (e.g., ${}^3\mathrm{He}{}^{-129}\mathrm{Xe}{}^{19}$), or precise characterization of the impurities.

The second major improvement is in the distance separating the polarized gas sample from the source mass. We will assume a cell with identical inner dimensions to the WK06 cell [Fig. 1(b)], but with a front window that is only 100 μ m thick. The separation between the cell and mass is assumed to be 50 μ m, for a total of

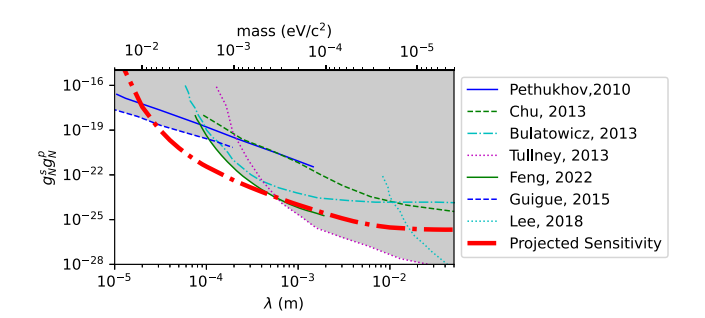


FIG. 5. Estimated sensitivity of a sideband-style measurement with 150 μ m spin-mass separation plus conditions as mentioned in the text compared to pre-existing experimental results (gray area).

150 μ m between the test mass and the nearest portion of polarized gas.

To estimate the sensitivity, we begin with the results of the ANGIS measurement campaign. Across all measurements, the mean statistical uncertainty in modulation depth was $\sigma(\Delta f)=0.405~\mu Hz.$ With an improved setup without the effects of magnetic impurities, we would expect a statistical distribution of values with a similar uncertainty but a near 0 frequency difference. With a measurement campaign of 100 runs, the statistical uncertainty would be reduced by a factor of 10,

$$\sigma(\Delta f) = \frac{0.405}{\sqrt{100}} \ \mu \text{Hz} = 0.0405 \ \mu \text{Hz}. \tag{14}$$

Combined with the simulated results and Eq. (12), we can then estimate the calculated $g_s^N g_p^n$ coupling constants for each distance scale. The contribution of the neutron to the ¹²⁹Xe spin is estimated using the expected shell model value.³⁹ Taking the 95% confidence interval results in improved experimental sensitivity for sub-millimeter distance scales, as shown in Fig. 5.

Further improvements should be possible in several ways. The relatively short T_2^* times of \approx 2800 s in these glued cells were limiting our total measurement time. T_2^* times of up to 8.5 h for ¹²⁹Xe as were achieved in blown glass cells within the BMSR-2³⁰ would allow to decrease the uncertainty within Eq. (14) by another factor of approximately three. With longer measurement durations, longer intervals for the stop positions of the wheel would also be possible, leading to much smaller modulation frequencies $f_{\rm m}$ and linearly increasing the sensitivity of our method. The problem of the increasing power of the sidelobes from the carrier signal could be addressed by an even better-adapted filter function before applying the DFT. In principle, our data would also allow for applying the global phase fit method, 40 which does not suffer from the sidelobe problem; however, one has to cut the data into small blocks and, thus, should have an overall lower sensitivity. Furthermore, the interaction strength could be increased by using materials whose densities differ more greatly than those of POM and germanium. Another more simple option would be to alternate between a high-density mass and air. As this would elevate the susceptibility effect, we excluded this approach. However, we have shown that this effect can be precisely simulated and experimentally studied. Only working with one piece of high-density

mass should also make it much easier to precisely clean it and, thus, eliminate effects from magnetized impurities.

SUPPLEMENTARY MATERIAL

In the supplementary material, more information is given on: (I) the influence of the transverse decay time T_2^\star and the noise floor level on the optimal measurement duration, (II) all measurements and experimental variations performed during the first test campaign, and (III) the three other distance dependence results.

See the supplementary material for the deduction of why a measurement duration in the length of T_2^* is giving the highest sensitivity.

ACKNOWLEDGMENTS

J. Shortino and W. M. Snow acknowledge support from US National Science Foundation (NSF) Grant Nos. PHY-1913789, PHY-2111347, and PHY-2209481 and the Indiana University Center for Spacetime Symmetries. J. Shortino also acknowledges the support of the German Academic Exchange Service (DAAD) through Program No. 57442045. P.-H. Chu acknowledges the Los Alamos National Laboratory LDRD office through Grant No. 20210750ECR.

We thank Dietmar Eberbeck for performing susceptibility measurements via MPMS and Tianhao Liu for simulating the magnetic field distortion from the test mass using COMSOL.

AUTHOR DECLARATIONS

Conflict of Interest

The authors have no conflicts to disclose.

Author Contributions

J. Shortino: Conceptualization (equal); Formal analysis (equal); Investigation (equal); Writing – original draft (lead); Writing – review & editing (equal). S. Knappe-Grueneberg: Conceptualization (equal); Formal analysis (supporting); Investigation (equal); Writing – review & editing (equal). J. Voigt: Conceptualization (equal); Formal analysis (supporting); Investigation (equal); Writing – review & editing (supporting); P.-H. Chu: Formal analysis (equal); Investigation (supporting); Writing – review & editing (equal). A. Reid: Conceptualization (supporting); Formal analysis (supporting); Investigation (supporting); Writing – review & editing (supporting); Investigation (supporting); Writing – review & editing (equal). W. Kilian: Conceptualization (equal); Formal analysis (supporting); Investigation (equal); Writing – review & editing (equal).

DATA AVAILABILITY

The data acquired during this study are available from the corresponding author upon reasonable request.

REFERENCES

- ¹J. Leitner and S. Okubo, "Parity, charge conjugation, and time reversal in the gravitational interaction," Phys. Rev. 136, B1542–B1546 (1964).
- ²C. T. Hill and G. G. Ross, "Models and new phenomenological implications of a class of pseudo-Goldstone Bosons," Nucl. Phys. B 311, 253–297 (1988).
- ³ J. Jaeckel and A. Ringwald, "The low-energy Frontier of particle physics," Annu. Rev. Nucl. Part. Sci. **60**, 405–437 (2010).
- ⁴A. Arvanitaki, S. Dimopoulos, S. Dubovsky, N. Kaloper, and J. March-Russell, "String axiverse," Phys. Rev. D **81**, 123530 (2010).
- ⁵K. Olive et al., "Review of particle physics," Chin. Phys. C 38, 090001 (2014).
- ⁶S. Weinberg, "Approximate symmetries and pseudo-goldstone bosons," Phys. Rev. Lett. **29**, 1698–1701 (1972).
- ⁷R. D. Peccei, "The Strong CP problem and axions," Lect. Notes Phys. **741**, 3–17 (2008).
- ⁸G. G. Raffelt, "Astrophysical axion bounds," in *Axions: Theory, Cosmology, and Experimental Searches*, edited by M. Kuster, G. Raffelt and B. Beltrán (Springer Berlin Heidelberg, Berlin, Heidelberg, 2008), pp. 51–71.
- ⁹J. Moody and F. Wilczek, "New macroscopic forces?," Phys. Rev. D **30**, 130–138 (1984).
- ¹⁰B. A. Dobrescu and I. Mocioiu, "Spin-dependent macroscopic forces from new particle exchange," J. High Energy Phys. 2006, 005.
- ¹¹P. Fadeev, Y. V. Stadnik, F. Ficek, M. G. Kozlov, V. V. Flambaum, and D. Bud-ker, "Revisiting spin-dependent forces mediated by new bosons: Potentials in the coordinate-space representation for macroscopic- and atomic-scale experiments," Phys. Rev. A 99, 022113 (2019).
- ¹² M. S. Safronova, D. Budker, D. DeMille, D. F. J. Kimball, A. Derevianko, and C. W. Clark, "Search for new physics with atoms and molecules," Rev. Mod. Phys. 90, 025008 (2018).
- ¹³ V. Flambaum and Y. Stadnik, "Searches for new particles including dark matter with atomic, molecular and optical systems," in *Springer Handbook of Atomic, Molecular, and Optical Physics*, edited by G. W. F. Drake (Springer International Publishing, Cham, 2023), pp. 461–469.
- ¹⁴ A. Arvanitaki and A. A. Geraci, "Resonantly detecting axion-mediated forces with nuclear magnetic resonance," Phys. Rev. Lett. 113, 161801 (2014).
- ¹⁵D. Budker, P. W. Graham, M. Ledbetter, S. Rajendran, and A. O. Sushkov, "Proposal for a cosmic axion spin precession experiment (CASPEr)," Phys. Rev. X 4, 021030 (2014).
- ¹⁶A. Garcon, D. Aybas, J. W. Blanchard, G. Centers, N. L. Figueroa, P. W. Graham, D. F. J. Kimball, S. Rajendran, M. G. Sendra, A. O. Sushkov, L. Trahms, T. Wang, A. Wickenbrock, T. Wu, and D. Budker, "The cosmic axion spin precession experiment (CASPEr): A dark-matter search with nuclear magnetic resonance," Quantum Sci. Technol. 3, 014008 (2017),
- ¹⁷A. Garcon, J. W. Blanchard, G. P. Centers, N. L. Figueroa, P. W. Graham, D. F. Jackson Kimball, S. Rajendran, A. O. Sushkov, Y. V. Stadnik, A. Wickenbrock, T. Wu, and D. Budker, "Constraints on bosonic dark matter from ultralow-field nuclear magnetic resonance," Sci. Adv. 5, eaax4539 (2019).
- ¹⁸P.-H. Chu, A. Dennis, C. B. Fu, H. Gao, R. Khatiwada, G. Laskaris, K. Li, E. Smith, W. M. Snow, H. Yan, and W. Zheng, "Laboratory search for spin-dependent short-range force from axion like particles using optically polarized ³He gas," Phys. Rev. D **87**, 011105 (2013).
- ¹⁹ K. Tullney, F. Allmendinger, M. Burghoff, W. Heil, S. Karpuk, W. Kilian, S. Knappe-Grüneberg, W. Müller, U. Schmidt, A. Schnabel, F. Seifert, Y. Sobolev, and L. Trahms, "Constraints on spin-dependent short-range interaction between nucleons," Phys. Rev. Lett. 111, 100801 (2013).
- ²⁰N. Aggarwal *et al.*, "Characterization of magnetic field noise in the ARIADNE source mass rotor," Phys. Rev. Res. **4**, 013090 (2022).
- ²¹ M. Bulatowicz, R. Griffith, M. Larsen, J. Mirijanian, C. B. Fu, E. Smith, W. M. Snow, H. Yan, and T. G. Walker, "Laboratory search for a long-range T-odd, P-odd interaction from axionlike particles using dual-species nuclear magnetic resonance with polarized ¹²⁹Xe and ¹³¹Xe gas," Phys. Rev. Lett. 111, 102001 (2013).
- ²²Y.-K. Feng, D.-H. Ning, S.-B. Zhang, Z.-T. Lu, and D. Sheng, "Search for monopole-dipole interactions at the submillimeter range with a ¹²⁹Xe-¹³¹Xe- Rb comagnetometer," Phys. Rev. Lett. **128**, 231803 (2022).

- ²³ E. Babcock, S. Boag, M. Becker, W. C. Chen, T. E. Chupp, T. R. Gentile, G. L. Jones, A. K. Petukhov, T. Soldner, and T. G. Walker, "Effects of high-flux neutron beams on ³He cells polarized *in situ* with spin-exchange optical pumping," Phys. Rev. A 80, 033414 (2009).
- ²⁴M. S. Albert, *Hyperpolarized and Inert Gas MRI*, edited by M. S. Albert and F. T. Hane (Academic Press, 2017).
- ²⁵ K. Slifer, M. Amarian, L. Auerbach, T. Averett, J. Berthot, P. Bertin, B. Bertozzi, T. Black, E. Brash, D. Brown *et al.*, "³He spin-dependent cross sections and sum rules," Physical review letters **101**, 022303 (2008).
- ²⁶J. L. Friar, B. F. Gibson, G. L. Payne, A. M. Bernstein, and T. E. Chupp, "Neutron polarization in polarized ³He targets," Phys. Rev. C 42, 2310–2314 (1990).
- ²⁷J. Engel, "Nuclear form factors for the scattering of weakly interacting massive particles," Phys. Lett. B 264, 114–119 (1991).
 ²⁸P. Toivanen, M. Kortelainen, J. Suhonen, and J. Toivanen, "Large-scale shell-
- ²⁸P. Toivanen, M. Kortelainen, J. Suhonen, and J. Toivanen, "Large-scale shell-model calculations of elastic and inelastic scattering rates of lightest supersymmetric particles (LSP) on ¹²⁷I, ¹²⁹Xe, ¹³¹Xe, and ¹³³Cs nuclei," Phys. Rev. C **79**, 044302 (2009).
- ²⁹C. Gemmel, W. Heil, S. Karpuk, K. Lenz, C. Ludwig, Y. Sobolev, K. Tullney, M. Burghoff, W. Kilian, S. Knappe-Grüneberg, W. Müller, A. Schnabel, F. Seifert *et al.*, "Ultra-sensitive magnetometry based on free precession of nuclear spins," Eur. Phys. J. D **57**, 303–320 (2010).
- ³⁰F. Allmendinger, W. Heil, S. Karpuk, W. Kilian, A. Scharth, U. Schmidt, A. Schnabel, Y. Sobolev, and K. Tullney, "New limit on Lorentz-invariance- and CPT-violating neutron spin interactions using a free-spin-precession ³He-¹²⁹Xe comagnetometer," Phys. Rev. Lett. **112**, 110801 (2014).
- ³¹ N. Sachdeva, I. Fan, E. Babcock, M. Burghoff, T. E. Chupp, S. Degenkolb, P. Fierlinger, S. Haude, E. Kraegeloh, W. Kilian, S. Knappe-Grüneberg, F. Kuchler,

- T. Liu, M. Marino, J. Meinel, K. Rolfs, Z. Salhi, A. Schnabel, J. T. Singh, S. Stuiber, W. A. Terrano, L. Trahms, and J. Voigt, "New measurement of the permanent electric dipole moment of ¹²⁹Xe using ³He comagnetometry and SQUID detection," Phys. Rev. Lett. **123**, 143003 (2019).
- ³²J. Voigt, *et al.*, (to be published).
- ³³ M. Limes, N. Dural, M. V. Romalis, E. Foley, T. Kornack, A. Nelson, L. Grisham, and J. Vaara, "Dipolar and scalar ³He-¹²⁹Xe frequency shifts in stemless cells," Phys. Rev. A **100**, 010501 (2019).
- $^{\bf 34}$ All gases had a purity of at least 4.8 i.e. 99.998% and were additionally fed via an O2 and H2O getter.
- ³⁵From the detected start amplitudes and the distance cell center to sensitive SQUID surface and the other experimental conditions one can estimate the 129Xe polarization after transport into the BMSR-2 to be in the range of 10%.
- ³⁶The sampling rate resulted from hardware constraints due to the combination of an external clock for the DAQ system and the anti aliasing filter chosen in the DAO system.
- ³⁷Y. J. Kim, P.-H. Chu, and I. Savukov, "Experimental constraint on an exotic spin- and velocity-dependent interaction in the sub-meV range of axion mass with a spin-exchange relaxation-free magnetometer," Phys. Rev. Lett. **121**, 091802 (2018).
- ³⁸Y. J. Kim, P.-H. Chu, I. Savukov, and S. Newman, "Experimental limit on an exotic parity-odd spin- and velocity-dependent interaction using an optically polarized vapor," Nat. Commun. 10, 2245 (2019).
 ³⁹D. F. J. Kimball, "Nuclear spin content and constraints on exotic spin-
- ⁵⁹D. F. J. Kimball, "Nuclear spin content and constraints on exotic spin-dependent couplings," New J. Phys. 17, 073008 (2015).
- ⁴⁰T. Liu, K. Rolfs, I. Fan, S. Haude, W. Kilian, L. Li, A. Schnabel, J. Voigt, and L. Trahms, "Revisiting ¹²⁹Xe electric dipole moment measurements applying a new global phase fitting approach," New J. Phys. **23**, 063076 (2021).